

NASA Technical Memorandum 105916

# On the Drag of Model Dendrite Fragments at Low Reynolds Number

R. Zakhem and P.D. Weidman  
*University of Colorado*  
*Boulder, Colorado*

and

H.C. de Groh III  
*Lewis Research Center*  
*Cleveland, Ohio*

February 1993

**NASA**

# ON THE DRAG OF MODEL DENDRITE FRAGMENTS AT LOW REYNOLDS NUMBER

by

R. Zakhem and P. D. Weidman  
Department of Mechanical Engineering  
University of Colorado  
Boulder, CO 80309

and

H. C. de Groh III  
NASA Lewis Research Center  
Materials Division, MS 105-1  
Cleveland, OH 44135

## ABSTRACT

An experimental study of low Reynolds number drag on laboratory models of dendrite fragments has been conducted. The terminal velocities of the dendrites undergoing free fall along their axis of symmetry were measured in a large Stokes flow facility. Corrections for wall interference give nearly linear drag versus Reynolds number curves. Corrections for both wall interference and inertia effects show that the dendrite Stokes settling velocities are always less than that of a sphere of equal mass and volume. In the Stokes limit, the settling speed ratio is found to correlate well with the primary dendrite arm aspect ratio and a second dimensionless shape parameter which serves as a measure of the fractal-like nature of the dendrite models. These results can be used to estimate equiaxed grain velocities and distance of travel in metal castings. The drag measurements may be used in numerical codes to calculate the movement of grains in a convecting melt in an effort to determine macrosegregation patterns caused by the sink/float mechanism.

## 1. INTRODUCTION

One of the most detrimental forms of segregation in metal castings is macrosegregation caused by the sinking (and floating) of free dendrites, equiaxed grains and inclusions. Movement of solid grains is fundamental to the formation and distribution of the equiaxed zone in castings<sup>[1,2,3]</sup>. The processing of monotectic alloys and particulate metal-matrix composites may also be limited due to Stokes flow and the redistribution of solid phases.<sup>[4]</sup> During solidification of an alloy the solid under formation is of a different composition than the liquid, provided the partition coefficient is not unity. Movement of either of these phases is required for the development of macrosegregation. The rate and manner by which the free solids settle will influence the amount and distribution of segregation. An understanding of this settling behavior is a necessary prelude to the understanding and possible control of the solidification process.

Segregation driven by a sink/float mechanism in the form of “kishing” of graphite flakes is common in the casting of cast iron<sup>[1]</sup> and is a factor in the solidification of Fe-C-Si alloys in low gravity,<sup>[5]</sup> and other eutectic systems.<sup>[6,7]</sup> Macrosegregation caused by this type of mechanism can be quite severe.<sup>[3,8,9]</sup> Free, unattached grains are produced by breakage of dendrites during pour casting<sup>[3]</sup> by partial remelting,<sup>[6,7]</sup> by mechanical disturbances such as stirring or vibration,<sup>[10-12]</sup> and by heterogeneous nucleation of grains in areas of high liquid fraction. Attempts have been made to use Stokes’ law to assist in the analysis of segregation caused by settling processes,<sup>[6,13]</sup> however a detailed study of the effects of grain geometry has not been reported.

The size and shape of settling dendrite fragments can be estimated from postsolidification microstructures. Three-dimensional dendrites can be thought of as simple constructions using cylindrical elements such as those shown in Fig. 1. The relative size and spacing of the primary and secondary arms are representative of numerous observations of real dendrite microstructures in Pb-Sn and are consistent with other morphology studies using Pb-Au and succinonitrile-acetone.<sup>[14,15]</sup> The nearly cylindrical dendritic fragments in Pb-Sn have diameters on the order of  $1-2 \times 10^{-5}$  m and lengths in the range  $2.5-8.0 \times 10^{-5}$  m<sup>[9]</sup>. These values were used to bound the aspect ratios of dendrite models studied here. Secondary arm spacing and average dendrite diameter measurements in Pb-Sn were used with the results of Tewari<sup>[14]</sup> to yield a parabolic tip radius to dendrite diameter ratio of 0.27. This relation was used to insure consistency between the shapes shown in Fig. 1, recent morphology studies, and measurements made in the Pb-Sn system.

An estimate of the dendrite Reynolds number in a casting can be obtained [cf. Eqn. (12)] by assuming a spherical dendrite of diameter  $d = 2a$  falls through the melt at its terminal velocity  $U_t = 2ga^2(\rho_s - \rho)/9\mu$ , where  $g$  is gravity,  $\rho_s$  is the density of the alloy solid, and  $\rho$  and  $\mu$  are the density and viscosity of the alloy melt, respectively. For a Pb-dendrite in a near eutectic alloy (62 wt.% Sn) with  $d = 4 \times 10^{-5}$  m,  $\rho_s = 1.13 \times 10^4$  kg/m<sup>3</sup>,  $\rho_\ell = 8.2 \times 10^3$  kg/m<sup>3</sup>, and  $\mu \cong 3 \times 10^{-3}$  kg/m-s one finds  $Re \cong 0.05$ . This may be regarded as an upper bound here because the maximum observed radius was used in the calculation, and perhaps for dendritic systems in general since Pb-Sn is characterized by a large density difference between the solid and melt. In any case, the expected Reynolds numbers are quite low and in many instances the dendrite may be considered to be in the Stokes flow regime. Also, owing to the small inertia effects, a free dendrite reaches its terminal velocity almost instantaneously, or at least in a time that is negligibly small compared to the average suspension time in any realistic casting system.

It is evident that the settling process can be very complicated. When a mold is filled the initial flow is highly turbulent. After the turbulent flow subsides, the movement of individual dendrites will be affected by neighboring dendrites and solid surfaces and collisions may take place. Even at low solid fractions, the motion of a single dendrite will be affected by convection currents induced by unstable thermal and concentration gradients in the liquid melt. In all cases the dendrite settling speed will depend on the orientation of its central axis with respect to the gravity vector. In this paper we do not address the above-mentioned complications, but rather focus attention on the settling velocity for dendrite models falling at steady terminal speed along their central axis at low Reynolds number in an unbounded fluid. Hence the present investigation represents a preliminary study of the very complex problem of dendrite motion in realistic solidification processing conditions. Introductory remarks given in Section 2 are followed by a description of the experimental apparatus and measurement procedure in Section 3. Drag and settling speed measurements reported in Section 4 are analyzed in terms of a nondimensional length scale which characterizes the fractal-like nature of the dendritic shapes. A discussion of results and concluding remarks are given in Section 5.

## 2. PRELIMINARY REMARKS

The drag on a sphere of radius  $R$  settling at constant speed  $U$  in an unbounded liquid of viscosity  $\mu$  in the limit of zero Reynolds number is given by<sup>[16]</sup>

$$D = 6\pi\mu RU. \quad (1)$$

One immediately observes that the characteristic force ( $\mu RU$ ) in Stokes flow is proportional to the viscosity. Thus a proper drag coefficient is obtained by normalization of the drag with  $\mu RU$  and not with a dynamic pressure proportional to the density as in a high Reynolds number flow. Stokes flow theory has been extensively developed for flow over long slender bodies and for flow past slightly deformed spheres, but results for more complicated shapes must be obtained by numerical integration of the governing equations of motion or by direct experimentation. In either case it is common procedure to report zero Reynolds number results in the form of the settling speed ratio<sup>[17]</sup>

$$KS = U_s / U_r, \quad (2)$$

where  $U_s$  is the Stokes velocity of the test object and  $U_r$  is the Stokes velocity of a reference sphere. The Stokes velocity is the settling speed of an object falling in an unbounded fluid in the limit of zero Reynolds number. The reference sphere is usually considered to be a sphere with mass and volume equal to that of the test object; in other words, it is the sphere formed by melting down the test specimen. When a body falls in a fluid at constant terminal velocity, its drag is equal to its weight less the buoyancy force of the displaced fluid. The submerged weight of a dendrite is therefore the dendrite drag in the present experiments. Since both the object and the reference sphere have the same weight and volume, they have the same drag. Hence the drag  $D$  on the object computed from Eqs. (1) and (2) may be written

$$D = D_r = 6\pi\mu a_r U_r = 6\pi\mu a_r U_s / KS, \quad (3)$$

where  $D_r$  is the reference sphere drag,  $U_r$  is its Stokes velocity,  $a_r = [3V/4\pi]^{1/3}$  is the radius of the reference sphere computed from the solid volume  $V$  of the test object. The settling speed ratio computed from Eq. (3) is then

$$KS = 6\pi\mu U_s a_r / D. \quad (4)$$

The goal of this study is to obtain the low Reynolds number variation of drag and the Stokes settling speed ratio  $KS$  for the model dendritic fragments given in Fig. 1. An accurate determination of  $KS$  thus depends on an accurate measurement of the parameters on the right hand side of Eq. (4).

It is clear that real experiments cannot be carried out at zero Reynolds number, and one must always be concerned with wall interference effects in any finite size experimental facility. These latter blockage corrections must be made to obtain the Reynolds number variation of drag in an unbounded fluid. The Stokes settling speed ratio  $KS$  is then obtained after making an additional correction for the effect of inertia in the finite Reynolds number experiments. The procedure for taking into account these corrections is presented in the following section.

### 3. EXPERIMENTAL SETUP AND MEASUREMENT PROCEDURE

#### A. Experimental Apparatus

The experiments were carried out in the Stokes facility reported in Lasso & Weidman.<sup>[18]</sup> The tank is composed of a thick aluminum base supporting vertical plate glass sidewalls 0.91 m high forming a square cross section  $L = 0.61$  m on edge. The large test facility was designed to permit the use of centimeter size test objects and yet achieve minimal sidewall blockage effects. The test facility is particularly well suited for objects of complicated shape which need to be of sufficient size to keep close tolerances on machining and construction. The tank is filled to a height of 0.85 m with 0.34 m<sup>3</sup> of Dow Corning 200 silicone oil with a nominal viscosity of  $2.5 \times 10^{-3}$  m<sup>2</sup>/s at room temperature. Currie and Smith<sup>[19]</sup> have shown that silicone oil at this viscosity is Newtonian for shear rates less than 150 s<sup>-1</sup>, well above the maximum shear rate 20 s<sup>-1</sup> estimated for the experiments reported here. The apparatus is equipped with a laser-triggered time interval measuring system accurate to 0.001 s, designed after the one used by Stalnaker and Hussey.<sup>[20]</sup> The release mechanism mounted on top of the tank consists of a ring supporting three Airpax Model K92121-P2 linear actuators located 120° apart, each equipped with needle-like prongs that can be radially positioned, independently or in unison, by means of an electronic controller. The centered prongs serve to align and hold the dendrite model along the tank's central axis. Subsequently, the assembly is lowered into the oil and the test object is released.

Prior to any experiment the silicone oil in the tank is mechanically mixed to overcome any temperature stratification induced by the ambient temperature gradient in the laboratory. Three hours after mixing, the temperature is found to vary less than 0.05 °C in the central region where tests are conducted.<sup>[18]</sup> An ASTM-56C Fisher mercury thermometer with 0.02 °C resolution was used to measure the fluid temperature in the center of the test region before and after a series of tests. All dendrite models were released along the tank centerline about 0.04 m below the free surface and fell approximately 0.23 m before intercepting the upper horizontal laser beam which triggers an electronic timer. The dendrite model falls an additional 0.2939 m before intercepting the second laser beam which records the transit time between the focused beams. The test object then settles to the bottom

of the tank approximately 0.28 m below the lower laser beam. Lasso and Weidman<sup>[18]</sup> found that test specimens of the size and weight used in the present investigation will be at their constant terminal speed during transit between the laser beams.

The variation of the fluid density  $\rho(T)$  and viscosity  $\mu(T)$  was measured over the range of temperatures incurred in the experiments. Details of these measurements are given in Appendix A. Least-squares fits to the data are given by

$$\rho = 1006.13 - 1.41 T \text{ (kg/m}^3\text{)} \quad (5)$$

$$\mu = 3.8216 - 0.05367 T \text{ (kg/m-s)} \quad (6)$$

valid in the temperature range  $20 \text{ }^\circ\text{C} < T < 27 \text{ }^\circ\text{C}$ .

Prior to weighing, all objects were cleaned in an ultrasonic bath and then allowed to dry at room temperature. Dry weight measurements were made with a Mettler Model H54 analytical balance having a resolution of  $\pm 0.01$  mg. The drag force was obtained by measuring the effective mass of the object immersed in a constant temperature bath of silicone oil and multiplying by the local gravitational acceleration ( $g = 9.79608 \text{ m/s}^2$ ). The drag was corrected to the temperature of the tank at the time of experimentation using<sup>[18]</sup>

$$D = D_o - gV \frac{d\rho}{dT} (T - T_o) = D_o + 1.41gV(T - T_o), \quad (7)$$

where  $D$  is the drag corrected to experimental temperature  $T$ , and  $D_o$  is the drag at temperature  $T_o$ . A direct calculation for the surface area  $A$  and volume  $V$  of each dendrite is given in Appendix B.

## B. Inertial and Blockage Correction Procedure

Eventhough the experimental facility is large, corrections for wall interference (blockage) effects are essential. Since the velocity in Stokes flow decays as the inverse power of the radial coordinate from the test object, a blockage ratio as small as 3% can induce a 10% error in the settling speed measurement from that in an unbounded fluid. Furthermore, all test objects have a finite Reynolds number and inertial corrections to obtain Stokes drag must also be made. These inertial effects typically become noticeable when the Reynolds number of the test object exceeds 0.1. Figure 2 depicts the essential features of the inertial and blockage correction procedure described below. The method equates the test object to a sphere of equal drag (effective weight in the test fluid), also having a zero Reynolds number blockage correction equal to that of a spheroid whose aspect ratio is determined by the maximum vertical and horizontal dimensions of the object. Use is made of the accurate experimental data of Sutterby<sup>[21]</sup> who measured wall interference and inertial corrections for spheres falling along the central axis of a concentric cylinder. Sutterby's correction constant  $K$  is defined as

$$K = U_s / U_m \quad (8)$$

where  $U_m$  is the measured settling velocity in a cylindrical tank and  $U_s$  is the Stokes velocity of the sphere. In order to make use of these results one must find the equivalent diameter,  $d_{eq}$ , for our tank of square section. The analysis of Happel & Bart<sup>[22]</sup> gives this relation to be

$$d_{eq} = 1.10659 L. \quad (9)$$

The specific steps comprising our generalized procedure for determining the wall interference and inertial corrections for axisymmetric or nearly axisymmetric bodies are as follows.

- (1) The maximum length  $\ell$  and maximum breadth  $b$  of the object [Fig. 2(a)] are determined. The length  $\ell$  is the maximum dimension of the body parallel to the vertical axis of free fall.
- (2) An equivalent spheroid [Fig. 2(b)] with semi-axes  $\ell/2$  and  $b/2$  along the vertical and horizontal axes, respectively, is constructed. This spheroid is an intermediate step that approximately accounts for the overall three-dimensional shape of the test object.
- (3) The spheroid fineness ratio  $\ell/b$  and its blockage ratio  $b/d_{eq}$  is computed. Using these geometric shape parameters, Table III of Wakiya<sup>[23]</sup> is interpolated to obtain the corresponding wall correction factor  $K_w$ . This is the blockage correction for a centrally falling spheroid that has the same fineness ratio ( $\ell/b$ ) as the experimental specimen. At this point finite Reynolds number blockage effects are approximately determined.
- (4) For the given value  $K_w$ , the  $Re = 0$  data in Table I of Sutterby<sup>[21]</sup> is quadratically interpolated and Eq. (9) is used to obtain the sphere blockage ratio  $d/d_{eq}$ . This blockage ratio corresponds to that of a sphere [Fig. 2(c)] with diameter  $d$  having the same zero Reynolds number wall interference effects as the equivalent spheroid.
- (5) This sphere becomes the *equivalent* sphere when it has the same drag as the test object. The Reynolds number,  $(Re)_{eq}$ , corresponding to this drag is estimated from the Stokes flow equation  $(Re)_{eq} = d^3 g \rho (\rho_s - \rho) / 18 \rho \mu^2$ , where  $\rho$  is the liquid density and  $\rho_s$  is the density of the solid dendrite. The equivalent sphere [Fig. 2(c)] now has the same drag and approximately the same zero Reynolds number blockage correction as the original test object [Fig. 2(a)].
- (6) Using the blockage ratio  $d/d_{eq}$  and Reynolds number  $(Re)_{eq}$ , Sutterby's<sup>[21]</sup> data is interpolated to obtain the combined inertial and wall correction constant  $K$  for the test object;

then the Stokes settling velocity  $U_s$  is computed from Eqn. (8).

It must be emphasized that the above “equivalent sphere method” correction procedure is approximate. However, a comparison of measurements with theoretical results for solid cylinders<sup>[18]</sup> indicate that it works well for axisymmetric test objects of moderate aspect ratio as in the present investigation.

### C. Dendrite Models

Four models of each dendritic shape sketched in Fig. 1 were constructed in order to cover a range of Reynolds numbers. Small and large models were each machined from Delrin and ABS (acrylonitrile-butadiene-styrene).

Delrin is heavier than ABS, so the drag and Reynolds number of the Delrin models are significantly larger than that of their ABS counterparts. Knowledge of the densities of the plastic models is not required in the data reduction. The models fall into two groups, uniaxial (U designation) and triaxial (T designation), and each group consists of branchless and branched models. The number immediately following the U or T designation denotes the number of sets of secondary branches. We distinguish between small and big, light and heavy geometrically similar models with letters S and B, L and H, respectively. Designation suffixes A, B, and C pertain to different primary rod aspect ratios  $\ell/a$  within a common group. The physical dimensions of each model are presented in Table I. Models for groups U0A, U2, U3, T0A, T0C, T1, and T2 were constructed to simulate actual dendrite shapes observed in metal alloys. Models for groups U0B and T0B were made at a later stage and tested to better understand trends in the experimental data. Models U1 were constructed at the last moment by removing the smaller set of secondary branches from two U2 models. In the end, a total of 34 model dendrites were constructed and tested.

#### 4. PRESENTATION OF RESULTS

Although the model dendrites were released with their primary axis of symmetry aligned with gravity, they sometimes tilted and rotated for reasons discussed in Lasso & Weidman.<sup>[18]</sup> Data was taken only if the central axis of a dendrite model exhibited a maximum declination of  $8^\circ$  from vertical and in most cases the angle of declination was less than  $3^\circ$ . The measured data for each dendrite presented in Table 11 include its dry mass  $M$ , the test temperature  $T$  of silicone oil, the dendrite drag (submerged weight)  $D$  at temperature  $T$ , and the measured terminal speed  $U_m$ . The next four columns list  $K_w$ ,  $d/d_{eq}$ ,  $(Re)_{eq}$  and  $K$  used to determine corrections for blockage and inertia effects as outlined in Section 3B. Next comes  $a_r$ , the radius of the sphere formed from the volume of the dendrite model, determined directly from the buoyancy measurements. The final two columns list the settling speed ratio  $KS$  and the dendrite Reynolds number defined as

$$Re = \frac{\rho a_r U_\infty}{\mu} \quad (10)$$

where  $U_\infty$  is the measured settling speed corrected only for blockage effects, *viz.*,  $U_\infty = K_w U_m$ .

The dendrite models may be distinguished by type (uniaxial or triaxial), complexity (the number of branch sets, with each set comprised of four orthogonally intersecting arms), and by the aspect ratio of the primary rods. Important geometric characteristics describing the models are given in Table III. The first column gives the designation for the dendrite models and the second column lists the average aspect ratio  $\ell/a$  of the vertical rods for each group determined from the dimensions in Table I. The next two columns give the volume and surface area of each dendrite computed from the results in Appendix B using the measurements in Table I. The following column gives  $a_r$  determined from the volume calculation in Appendix B, and one should note that these results agree well with the corresponding values for  $a_r$ , given in Table II obtained from the buoyancy measurements.

The Reynolds number variation of dendrite drag for all test specimens is plotted in log-log form in Fig. 3. It should be mentioned that in these drag curves, both the drag and the Reynolds numbers have been adjusted to a common temperature  $T = T_r = 24.4^\circ\text{C}$ , necessary for a consistent comparison since the drag has not been nondimensionalized. These values of  $D(T_r)$  and  $Re(T_r)$  are listed in Table III. We note that the data for model

UI was obtained using a different silicone oil with kinematic viscosity  $\nu = 2.41 \times 10^{-3} \text{ m}^2/\text{s}$  (@  $T_p$ ) and its Reynolds number was made consistent via the equation  $\text{Re}_2 = (\nu_1 \mu_1 / \nu_2 \mu_2) \text{Re}_1$ . Individual drag curves for each model are presented in Fig. 4 with quadratic least-squares fits through the origin. Error bars represent the rms deviation of repeated (two to three) measurements. The error range is because of the scatter in the fall time which varies with dendrite declination from vertical ( $\leq 8^\circ$ ). The curve fits in Fig. 4(a) are all closely linear, attesting to the fact that inertia effects are unimportant when  $\text{Re} < 0.1$ . Curve fits to the higher Reynolds number data in Fig. 4(b), on the other hand, do exhibit slight nonlinearity. For example, the dashed line for dendrite TOB is a linear fit through the origin for the lower data point, while the quadratic fitted curve exhibits a clear rise above the linear drag line. Each curve in Fig. 4(b) shows that inertial effects first become apparent for these dendrite models when  $\text{Re} > 0.1$ , approximately. However, even if the Reynolds number is as high as 0.4, the results in Fig. 4(b) show that only a small deviation from Stokes drag behaviour on the order of 5-10% would be encountered. Our choice of weights and sizes of the model dendrites did not uniformly span the range of Reynolds numbers in each group; the Reynolds number for two models (SH and BL) are nearly the same. The close correspondence between the values of drag for these widely disparate (but geometrically similar) models of nearly equal Reynolds numbers provides validation of Reynolds' similarity law. Thus the present results are valid for any dendrite mass of similar geometry as long as it falls within the range of Reynolds numbers tested.

The average value of the Stokes settling speed ratio  $\text{KS}$  computed from Eq. (4) for each of the ten dendrite groups are given in Table III.  $\text{KS}$  is, by definition, Reynolds number independent and thus depends only on the aspect ratio of the axial rods and the complexity of the dendrite configuration. As a measure of the fractal-like nature of the dendrites, we introduce the shape length scale  $L_s = 3V/A$  which decreases with increasing dendrite complexity. This choice of length scale is motivated by the fact<sup>[24]</sup> that the Stokes drag of a sphere is one-third volume dependent (pressure drag) and two-thirds area dependent (viscous drag) and hence the Stokes drag on bodies of greatly varying volume/area ratio is expected to depend on this quantity. The length scale is made nondimensional by  $a_p$  so that the parameter  $L_s/a_p$  takes on the value unity for a sphere and decreases with increasing dendrite complexity. Indeed<sup>†</sup>, this parameter is not new since Wadell<sup>[25]</sup> introduced it nearly 60 years ago calling it  $\psi$ , the ‘‘degree of true sphericity’’, defined as the surface area of a volume-equivalent sphere divided by the surface area of the test particle and hence  $\psi = L_s/a_p$ . The calculated values of  $L_s$  and the average dimensionless shape parameter  $a_p/L_s (= \psi^{-1})$  are listed in Table III. Figure 5 gives a plot of the settling speed ratio  $\text{KS}$  as a function of  $a_p/L_s$ , with rod aspect ratio  $\ell/a$  as a parameter. Circles and triangles correspond to uniaxial and triaxial dendrite models, respectively, and the open symbols refer to branchless dendrites while the closed symbols denote branched systems. Again vertical error bars represent the rms deviation in repeated measurements. The data falls neatly into two groups, triaxial and uniaxial, with the settling speed of the triaxial dendrites consistently lower than that for uniaxial dendrites of the same aspect ratio. Clearly, the horizontal rods of the triaxial models offer more resistance and result in a lower value of  $\text{KS}$ . The effect of secondary branches at fixed aspect ratio is shown by the dashed lines which follow  $\ell/a \cong 4$  for the uniaxial models and  $\ell/a \cong 8$  for the triaxial models. In both cases the settling speed ratios appear to asymptote to constant values as the branching patterns become more complex. The asymptotic values are approximately  $\text{KS} \cong 0.8$  for uniaxial models with  $\ell/a \cong 4$  and  $\text{KS} \cong 0.6$  for triaxial models with  $\ell/a \cong 8$ . These results show that the more realistic dendrite shapes (triaxial with secondary branching) have settling speeds 40% lower than spheres of equal mass.

---

<sup>†</sup>The authors are indebted to Mr. Sandeep Ahuja for bringing this fact to our attention.

Following Heiss and Coull,<sup>[26]</sup> an alternative procedure to correct for inertia effects is to extrapolate the drag curves back to zero Reynolds number. We define the zero Reynolds number drag coefficient  $C_d$  as

$$C_d = \frac{\left. \frac{d(D)}{d(\text{Re})} \right|_{\text{Re}=0}}{6\pi\mu\nu} \quad (11)$$

and note that the numerator in this expression is readily determined from the quadratic least-squares fits to the individual drag curves in Fig. 4. This direct approach may constitute a more accurate way of determining Stokes drag results because only the blockage correction factor  $K_w$  is used and the slope calculation emphasizes the data in the linear regime  $\text{Re} < 0.1$  where  $K_w$  is small (cf. Table II). The drag coefficients are listed in Table III and plotted as a function of the dimensionless shape parameter in Fig. 6 with the same definitions for the symbols as in Fig. 5. The branchless uniaxial and triaxial data exhibit a linear variation drag coefficient with  $a_f/L_s$ . Also, as expected, the drag slope of the triaxial models is greater than that of the uniaxial ones. The effect of adding secondary branches is to move along the dashed curves to asymptotic values  $C_d \cong 1.2$  for uniaxial dendrites of aspect ratio  $\ell/a \cong 4$  and  $C_d \cong 1.7$  for triaxial dendrites of aspect ratio  $\ell/a \cong 8$ . In the limit  $\text{Re} \rightarrow 0$ ,  $U_\infty \rightarrow U_s$ , and Eq. (3) gives  $D = 6\pi\mu\nu\text{Re}/\text{KS}$ . It then follows from Eq. (12) that  $C_d = (\text{KS})^{-1}$ . Thus the extrapolation procedure for calculating the zero Reynolds number drag coefficient  $C_d$  provides an alternate method for calculating KS. The consistency of the two independent determinations of KS is seen in Fig. 7 where a plot of  $C_d$  versus  $(\text{KS})^{-1}$  reveals a straight line nearly within experimental error.

## 5. DISCUSSION AND CONCLUSION

Plastic dendrite models patterned after the shapes of real dendritic fragments observed in postsolidification microstructures of metallic alloys were constructed for testing in a low Reynolds number experimental apparatus. The settling speeds of 34 models conforming to four uniaxial and the three triaxial configurations of varying aspect ratio were measured. The blockage-corrected drag curves for these models given in Fig. 4 exhibit noninertial behavior when  $\text{Re} < 0.1$  and inertial effects become evident when  $\text{Re} > 0.1$ . Results in the Stokes flow limit of zero Reynolds number have been derived by two independent means. In the first method, the *ad hoc* procedure of Lasso and Weidman<sup>[18]</sup> is used to estimate inertial corrections to determine KS, the Stokes settling speed ratio defined by Eq. (2). In the second method, the blockage-corrected drag curves were used to determine the zero Reynolds number drag coefficient given by Eq. (11), itself equivalent to the inverse of KS. The consistency of the two approaches is verified in Fig. 7, but it is believed that the direct extrapolation of the drag data provides somewhat more accurate results when sufficient data at low Reynolds number are available. Figures 5 and 6 show that the Stokes results for these complex dendrite fragments correlate well with the dimensionless shape parameter  $a_f/L_s$ .

The results in Figs. 5 and 6 show that the settling speed KS and drag coefficient  $C_d$  for dendrites in real metal casting systems will have values significantly different from spheres of equal mass (unity for both KS and  $C_d$ ). In particular, at large  $a_f/L_s$ , uniaxial dendrites with  $\ell/a \cong 4.0$  have settling speeds 20% slower than equal mass spheres and triaxial dendrites with  $\ell/a \cong 8.0$  have settling speeds 40% slower. Figures 5 and 6 also show that secondary branching has profoundly different effects on the uniaxial and triaxial dendrite models. The growth of

secondary branches on uniaxial models of aspect ratio  $\ell/a \cong 4$  causes an immediate increase in the drag coefficient and concomitant decrease in KS. Secondary branching on the triaxial models of aspect ratio  $\ell/a \cong 8$ , on the other hand, exhibits no discernible effect on the dendrite drag. The explanation for this difference in behavior is as follows. The addition of secondary arms to the uniaxial fragments greatly increases the horizontal scale of the dendrite and hence its drag. Further addition of smaller secondary arms do not increase the horizontal scale of the fragment and offer little (if any) increase in  $C_d$ . The slight increase in the drag coefficient for branched uniaxial dendrites in Fig. 6 is most likely due to the increase in aspect ratio of the models from 3.8 to 4.4. In the case, of triaxial dendrites, the growth of secondary branches is observed to have virtually no effect on the drag coefficient, the slight differences in  $C_d$  with secondary branching again being attributed to the different aspect ratios of the primary rods. This is due to the fact that secondary branching on a triaxial model does not alter its horizontal length scale which is already set by the branchless configuration. It is possible that a more accurate set of measurements would exhibit some slight change in the drag coefficient when secondary branches of dendritic form are added to the basic triaxial stalk, but the measurements presented here suggest that secondary branching on triaxial dendrites will not affect the settling speed ratio.

One must bear in mind that the foregoing results depend only on the Reynolds number of the dendrite and its shape as characterized by the nondimensional parameters  $\ell/a$  and  $a_r/L_s$ . The foregoing results may be used to estimate the settling rate of a low Reynolds number dendrite fragment in a metal casting as follows. First the dendrite model shape most similar to grains observed in the casting is chosen from Fig. 1. Next the values of the shape parameters  $\ell/a$  and  $a_r/L_s$  are estimated through analysis of dendrite size and back of the envelope calculations for dendrite models composed of mutually intersecting rods. The corresponding settling speed ratio KS is then found from the results in Fig. 5. Finally, Stokes' law gives the terminal velocity

$$U_s = \text{KS } U_r = \frac{2}{9} \left( \frac{a_r^2 g \Delta\rho}{\mu} \right) \text{KS} \quad (12)$$

where  $g$  is the local gravitational constant and  $\Delta\rho$  is the density difference between the solid dendrite and its liquid surrounding. (Note that the dendrite mass enters through the term  $\Delta\rho$ .) Thus the values of KS provided in this study enable one to ascertain meaningful estimates of the velocity, and hence distance of travel, for dendrite fragments and equiaxed grains in solidifying metal alloys under ideal conditions in the absence of convection. In closing, however, we note that the drag coefficient curves may be input into numerical codes to calculate the movement of dendrite fragments in a convecting melt, and thereby obtain particle trajectories and settling times in more realistic solidification processes.

## ACKNOWLEDGMENTS

The authors are grateful to Karl Rupp and Karl Gebert for their painstakingly accurate construction of the complicated dendrite models. We thank Dow Corning Corporation and the Lewis Microgravity Materials Science Laboratory for donations of silicone oil used in the experiments. We also acknowledge Storage Technology Corporation for use of their Brookfield viscometer.

## APPENDIX A: Density and Viscosity Measurements

The density of the silicone oil was measured using a Mettler/Parar model DMA40 digital density meter. The measuring principle is based on the natural frequency of oscillation of a fluid-filled glass U-tube. The mass, and hence the density, of the test fluid in the U-tube affects the natural frequency of the oscillating, liquid filled U-tube. In practice the density is calculated from the equation

$$\rho = A(R^2 - B) \quad (A1)$$

where  $\rho$  is the density in  $\text{kg/m}^3$ ,  $R$  is the digital readout of the instrument, and  $A$  and  $B$  are calibration constants determined by taking readings for liquids or gases of well-known densities. These constants were determined using air and distilled water as the calibration fluids. The density meter was connected to a constant temperature bath regulated by a Yellow Springs Model 72 temperature controller. The bath circulates water at nearly constant temperature ( $\pm 0.01$  °C during time of measurement) through a glass tube enclosing the vibrating U-tube. The absolute air pressure in the room was measured to the nearest 0.5 Torr by means of an MKS Baratron Model 220BA absolute pressure transducer. An analysis of sources of error gives a maximum density error of 0.05% for densities near unity. The measured densities of the silicone oil over a range of temperatures are presented in Fig. A1. Open and solid symbols correspond to measurements made before and after the 18 month period of data acquisition, respectively. It is clear that the density is very nearly a linear function of temperature over the range of interest and a linear least-squares fit shown in the figure is given by Eq. (5) in Section 3A.

The absolute viscosity of the silicone oil was measured using a Model DV-II Brookfield Digital Viscometer. Although not quite as accurate as a factory calibrated Cannon-Fenske viscometer used for measuring kinematic viscosity, proper cone selection and experience showed that repeatable measurements with error on the order of 0.5% is expected. Silicone oil viscosity measurements taken before and after the 18 month period of the experiment are plotted in Fig. A2. The linear least-squares fit shown in the figure is given by Eq. (6) in Section 3A.

## APPENDIX B: Calculation of Dendrite Volume and Area

The mathematical determination of the volume and surface area of the dendrite models is not a trivial matter. Clearly, the total volume and area for a dendrite composed of intersecting cylinders with hemispherical ends are less than the volume and area of the nonintersecting cylinders used in their construction, and one needs to ascertain the common volume and masked area in regions of intersection. Figure B1 displays two types of mutual intersections of three cylinders. In Fig. B1(a) a cylinder of radius  $R_2$  is symmetrically pierced by two orthogonally intersecting cylinders of smaller radii  $R_1$ . In Fig. B1(b) three cylinders of equal radii  $R_2$  mutually intersect at the origin of the Cartesian coordinate system. We write  $V_{1/2}$  for the volume of cylinder 1 displaced by cylinder 2;  $A_{1/2}$  is the area of cylinder 1 masked by cylinder 2; etc. Note that in general  $A_{1/2} \neq A_{2/1}$ .

Consider first the problem of the orthogonal intersection of a single cylinder of radius  $R_1$  along the y-axis with a larger cylinder of radius  $R_2$  along the z-axis as shown in Fig. B1. The cylindrical surfaces are described by the equations

$$x^2 + z^2 = R_1^2, \quad x^2 + y^2 = R_2^2. \quad (\text{B1})$$

The following expression for  $V_{1/2}$  may be integrated once to obtain

$$V_{1/2} = 8 \int_0^{R_1} dz \int_0^{x(z)} y(x) dx = 4 I_1 + 4 R_2^2 I_2, \quad (\text{B2})$$

where

$$I_1 = \int_0^{R_1} \sqrt{(R_2^2 - R_1^2)R_1^2 + (R_2^2 - 2R_1^2)z^2 - z^4} dz = \frac{R_2}{3} \left[ (R_2^2 - R_1^2)\bar{F}(m) - (R_2^2 - 2R_1^2)\bar{E}(m) \right] \quad (\text{B3})$$

$$I_2 = \int_0^{R_1} \arcsin\left(\frac{\sqrt{R_1^2 - z^2}}{R_2}\right) dz = 4R_1R_2^2 \left[ m^{-1/2}E(\phi^* | m) + (m-1)F(\phi | m) \right]. \quad (\text{B4})$$

Here  $\bar{F}(m)$  and  $\bar{E}(m)$  are complete elliptic integrals of the first and second kind, respectively, with modulus  $m = R_1^2/R_2^2$ . In Eq. (B4)  $\phi = \sin^{-1} \sqrt{m}$  and  $\phi^*$  is defined through the relation

$$F(\phi | m) = m^{1/2}F(\phi^* | m). \quad (\text{B5})$$

$I_2$  was calculated by the change variables  $\sin\theta = \sqrt{R_1^2 - y^2}/R_2$  and subsequent integration by parts yielding an incomplete elliptic integral of the second kind with modulus greater than unity. Using identities in Abramowitz & Stegun,<sup>[27]</sup> the result was rewritten in standard form with modulus less than unity. Combining results one obtains the common volume for two intersecting cylinders as

$$V_{1/2} = \frac{4R_2^3}{3} \left[ (1-m)\bar{F}(m) - (1-2m)\bar{E}(m) \right] + 4R_2^3 \left[ E(\phi^* | m) + m^{-1/2}(m-1)F(\phi | m) \right]. \quad (\text{B6})$$

Consider now the computation of masked areas. Referring again to Fig. B1 the area of cylinder  $R_1$  masked by cylinder  $R_2$  is given by

$$A_{1/2} = 8 \int_0^{\pi/2} \sqrt{(R_2^2 - R_1^2) + R_1^2 \sin^2 \theta_1} R_1 d\theta_1 = 8R_1R_2\bar{E}(m) \quad (\text{B7})$$

where  $\theta_1$ , is the azimuthal coordinate for the smaller cylinder. The area of cylinder  $R_2$  masked by cylinder  $R_1$  is given by

$$A_{2/1} = 8 \int_0^\phi \sqrt{R_1^2 - R_2^2 \sin^2 \theta_2} R_2 d\theta_2 = 8R_1R_2 \left[ m^{-1/2}E(\phi^* | m) + m^{-1}(m-1)F(\phi | m) \right] \quad (\text{B8})$$

where  $\theta_2$  is the azimuthal coordinate for the larger cylinder and  $\phi$  is defined above. Thus the total masked surface area for two orthogonally intersecting cylinders is given by

$$\Delta A_{1/2} = A_{1/2} + A_{2/1} = 8R_1R_2 \left[ \bar{E}(m) + m^{-1/2}E(\phi^* | m) + m^{-1}(m-1)F(\phi | m) \right]. \quad (\text{B9})$$

The overlapping volume and area for three orthogonally intersecting cylinders two of radii  $R_1$  and the third of radius  $R_2 > R_1$  may now be calculated. We note in Fig. 1 in Section 1 that the smaller cylinders do not intersect each other *outside* the boundary of the larger cylinder. In this case  $R_1 \leq R_2/\sqrt{2}$ , and the reduced volume due to mutual intersection is simply twice  $V_{1/2}$ . We denote this volume as  $\Delta V_{1/1/2}$ , and hence

$$\Delta V_{1/1/2} = \frac{8R_2^3}{3} \left[ (1-m)\bar{F}(m) - (1-2m)\bar{E}(m) \right] + 8R_2^3 \left[ E(\phi^* | m) + m^{-1/2}(m-1)F(\phi | m) \right]. \quad (\text{B10})$$

Similarly, the total masked area of the three intersecting cylinders denoted as  $\Delta A_{1/1/2}$  is simply twice  $\Delta A_{1/2}$ , and substituting  $m = R_1/R_2$  into (B9) yields

$$\Delta A_{1/1/2} = 16R_2^2 \left[ m^{1/2}\bar{E}(m) + E(\phi^* | m) + m^{-1/2}(m-1)F(\phi | m) \right]. \quad (\text{B11})$$

Consider lastly the special case of three orthogonally intersecting cylinders of equal radii  $R$  as shown in Fig. B2. The volume common to two intersecting cylinders can be determined by setting  $R_1 = R_2$  in Eq. (B6) and taking the limit  $m \rightarrow 1$  which yields

$$V_{2/2} = 16R_2^3 / 3. \quad (\text{B12})$$

When a third cylinder perpendicularly intersects these two cylinders as in Fig. B2, the volume of the third cylinder displaced by the other two is given by

$$V_{2/2/2} = 16 \int_0^{\pi/4} \int_0^{R_2} \sqrt{R_2^2 - r^2 \sin^2 \theta} \, r dr d\theta = \frac{16}{3} R_2^3 \left( \frac{3\sqrt{2}}{2} - 1 \right). \quad (\text{B13})$$

The total displaced volume for three mutually intersecting cylinders of equal radii  $R_2$  is then

$$\Delta V_{2/2/2} = V_{2/2} + V_{2/2/2} = 8\sqrt{2} R_2^3. \quad (\text{B14})$$

The area of a single cylinder masked by the two other intersecting cylinders in Fig. B2 is given by

$$A_{2/2} = 8 \int_{\pi/4}^{\pi/2} R_2^2 \sin \theta \, d\theta = 8\sqrt{2} R_2^2, \quad (\text{B15})$$

and the masked area of the three orthogonally intersecting cylinders is readily found to be

$$\Delta A_{2/2/2} = 3 A_{2/2} = 24\sqrt{2} R_2^2. \quad (\text{B16})$$

The volume and its surface area of a dendrite model can now readily be determined. Suppose the dendrite is composed of  $m$  triple intersections of cylinders of equal radii  $R_2$  and  $n$  mutual intersections of two cylinders of radii  $R_1$  with one of the larger cylinders of radius  $R_2$ . The volume and surface area of that dendrite is given by

$$V = \Sigma V_{1,2} - m \Delta V_{2/2/2} - n \Delta V_{1/1/2} \quad (\text{B17})$$

$$A = \Sigma A_{1,2} - m \Delta A_{2/2/2} - n \Delta A_{1/1/2} \quad (\text{B18})$$

where  $\Sigma V_{1,2}$  is the sum of the volumes and  $\Sigma A_{1,2}$  is the sum of the surface areas of all the individual nonintersecting cylinders of radii  $R_1$  and  $R_2$  which make up the dendrite. Extensions of this methodology to dendrites with systems of smaller branches is straight forward.

## REFERENCES

1. P. A. Curreri and D. M. Stefanescu: *Metals Handbook*, 9th Ed., Volume 15: Casting. ASM International, Metals Park, OH, 1988, pp. 147-158.
2. M. C. Flemings: *Solidification Processing*, McGraw-Hill, New York, NY, 1974, pp. 244-245.
3. R. T. Southin: *Trans. Met. Soc. AIME*, 1967, vol. 239, pp. 220-225.
4. A. Ohno: *Solidification: The Separation Theory and its Practical Application*, Springer-Verlag, Berlin, 1987, pp. 17-18, 44, 112.
5. D. M. Stefanescu, P. A. Curreri and R. Fiske: *Met. Trans. A*, 1986, vol. 17A, pp. 1121-1130.
6. B. C. Allen and S. Isserow: *Acta Met.*, 1957, vol. 5, pp. 465-472.
7. T. E. Strangman and T. Z. Kattamis: *Metall. Trans.*, 1973, vol. 4, pp. 2219-2221.
8. H. C. de Groh III and V. Laxmanan: *Metall. Trans. A*, 1988, vol. 19A, pp. 2651-2658.
9. H. C. de Groh III and V. Laxmanan: *Solidification Processing of Eutectic Alloys*, TMS-AIME, Warrendale, PA, 1988, pp. 229-242.
10. P. D. Southgate: *J. Metals*, 1957, vol. 9, No. 4, pp. 514-517.
11. A. N. Turner: *J. Metals*, 1957, vol. 9, No. 10, pp. 1295-1296.
12. R. T. Southin: *Trans. Met. Soc. AIME*, 1968, vol. 242, pp. 2240-2241.
13. F. Weinberg: *Metall. Trans. B*, 1984, vol. 15B, pp. 479-485.
14. S. N. Tewari, V. V. Nesarikar and D. Lee: *Metall. Trans. A*, 1989, vol. 20A, pp. 1889-1893.
15. K. Somboonsuk, J. T. Mason and R. Trivedi: *Metall. Trans. A*, 1974, vol. 15A, pp. 967-975.
16. G. G. Stokes: *Trans. Camb. Phil. Soc.*, 1845, vol. 8, pp. 287-319.
17. G. K. Youngren and A. Acrivos: *J. Fluid Mech.*, 1975, vol. 69, pp. 377-403.
18. I. Lasso and P. D. Weidman: *Phys. Fluids*, 1986, vol. 29, pp. 3921-3934.
19. C. C. Currie and B. F. Smith: *Ind. Eng. Chem.*, 1950, vol. 42, pp. 2457-2461.
20. J. F. Stalnaker and R. G. Hussey: *Phys. Fluids*, 1979, vol. 22, pp. 603-613.
21. J. L. Sutterby: *Trans. Soc. Rheol.*, 1973, vol. 17, pp. 559-573.
22. J. Happel and E. Bart: *Appl. Sci. Res.*, 1974, vol. 29, pp. 241-258.

23. S. Wakiya: J. Phys. Japan, 1957, vol. 12, pp. 1130-1141.
24. J. Happel and H. Brenner: Low Reynolds number hydrodynamics, Noordhoff International Publishing, Leyden, The Netherlands, 1973, p. 122.
25. H. Wadell: J. Geol., 1933, vol. 41, pp. 310-331.
26. J. F. Heiss and J. Coull: Chem. Engr. Prog., 1952, vol. 48, pp. 133-140.
27. M. Abramowitz and I. A. Stegun: Handbook of Mathematical Functions, National Bureau of Standards, Applied Mathematics Series 55, U. S. Govt. Printing Office, Washington D.C., 1972, pp. 589-626.

Model	$l$	$a$	$a'$	$b$	$b'$	$b''$	$c$	$c'$	$c''$
U0A S	2.223	0.635	-	-	-	-	-	-	-
U0A B	4.709	1.270	-	-	-	-	-	-	-
U0B S	2.540	0.318	-	-	-	-	-	-	-
U0B B	5.080	0.635	-	-	-	-	-	-	-
U1 S	2.413	0.635	0.228	1.905	-	-	0.762	-	-
U1 B	4.826	1.270	0.482	3.810	-	-	1.524	-	-
U2 S	2.413	0.635	0.228	1.905	1.466	-	0.762	1.143	-
U2 B	4.826	1.270	0.482	3.810	2.934	-	1.524	2.286	-
U3 S	2.794	0.635	0.228	2.032	1.905	1.466	0.762	1.143	1.524
U3 B	5.588	1.270	0.482	4.064	3.810	2.934	1.524	2.286	3.048
T0A S	2.540	0.956	-	2.540	-	-	-	-	-
T0B B	5.080	1.270	-	5.080	-	-	-	-	-
T0C S	2.540	0.318	-	2.540	-	-	-	-	-
T0C B	5.080	0.635	-	5.080	-	-	-	-	-
T1 S	2.350	0.318	0.122	2.350	0.732	-	-	0.635	-
T1 B	4.699	0.635	0.228	4.699	1.466	-	-	1.270	-
T2 S	2.743	0.318	0.122	2.743	0.953	0.732	-	0.635	0.826
T2 B	5.486	0.635	0.228	5.486	1.905	1.466	-	1.270	1.651

**Table I** Physical dimensions of the ten groups of dendrite models. All dimensions are in units of  $10^{-2}$  meters.

Model	M	D	T	$U_m$	$K_w$	$d/d_e$	$(Re)_{eq}$	K	$a_r$	KS	Re
	$10^{-3}$ kg	$10^{-5}$ N	$^{\circ}C$	$10^{-2}$ m/s					$10^{-2}$ m		
U0A SL	0.706	42.12	24.7	0.140	1.028	0.0130	0.0066	1.026	0.546	0.877	0.00306
U0A SH	0.918	280.16	24.7	0.995	1.028	0.0130	0.0451	1.030	0.538	0.927	0.02139
U0A BL	5.660	365.39	24.7	0.596	1.059	0.0266	0.0602	1.063	1.091	0.892	0.02679
U0A BH	7.487	2256.00	24.7	3.573	1.059	0.0266	0.3760	1.089	1.084	0.881	0.15955
U0B SL	0.201	10.78	23.1	0.049	1.014	0.0066	0.0016	1.011	0.360	0.814	0.00068
U0B SH	0.279	87.19	23.1	0.391	1.014	0.0066	0.0134	1.012	0.360	0.796	0.00538
U0B BL	1.606	99.92	23.1	0.214	1.028	0.0130	0.0146	1.023	0.718	0.765	0.00594
U0B BH	2.214	690.62	23.1	1.497	1.028	0.0130	0.1070	1.033	0.718	0.783	0.04167
U1 SL	0.838	43.10	24.7	0.142	1.067	0.0297	0.0069	1.066	0.580	0.836	0.00411
U1 BL	6.635	374.20	24.7	0.576	1.144	0.0598	0.0062	1.148	1.154	0.835	0.03556
U2 SL	0.919	50.94	23.1	0.128	1.067	0.0297	0.0075	1.066	0.597	0.781	0.00308
U2 SH	1.211	362.45	24.7	0.977	1.067	0.0297	0.0593	1.070	0.591	0.804	0.02398
U2 BL	7.275	414.37	23.1	0.528	1.144	0.0598	0.0611	1.148	1.190	0.846	0.02707
U2 BH	9.928	2966.20	24.7	3.622	1.144	0.0598	0.4800	1.163	1.193	0.798	0.19209
U3 SL	1.134	63.67	25.4	0.154	1.073	0.0323	0.0104	1.073	0.641	0.774	0.00419
U3 SH	1.528	456.49	24.7	1.117	1.073	0.0323	0.0748	1.076	0.639	0.793	0.02979
U3 BL	9.331	470.21	24.7	0.547	1.157	0.0648	0.0744	1.164	1.296	0.826	0.03189
U3 BH	12.55	3736.20	24.7	3.883	1.157	0.0648	0.6120	1.182	1.290	0.746	0.22546
T0A SL	3.684	224.33	24.7	0.389	1.089	0.0387	0.0420	1.088	0.909	0.809	0.01498
T0A SH	5.066	1494.80	24.7	2.540	1.089	0.0387	0.2400	1.099	0.955	0.840	0.10267
T0B BL	15.49	984.50	24.7	0.833	1.189	0.0760	0.1620	1.194	1.527	0.728	0.05884
T0B BH	21.22	6409.50	24.7	5.273	1.189	0.0760	1.0300	1.230	1.534	0.731	0.37400
T0C SL	0.553	29.39	23.1	0.065	1.089	0.0387	0.0042	1.086	0.505	0.592	0.00134
T0C SH	0.756	227.26	23.1	0.499	1.089	0.0387	0.0350	1.087	0.505	0.586	0.01033
T0C BL	4.410	244.90	23.1	0.247	1.189	0.0760	0.0340	1.176	1.007	0.582	0.01115
T0C BH	6.068	1860.20	23.1	1.889	1.189	0.0760	0.2600	1.179	1.008	0.587	0.08530
T1 SL	0.561	31.35	25.4	0.076	1.081	0.0355	0.0052	1.078	0.507	0.623	0.00166
T1 SH	0.778	222.37	24.7	0.520	1.081	0.0355	0.0360	1.080	0.514	0.611	0.01122
T1 BL	4.412	232.16	25.4	0.255	1.173	0.0704	0.0395	1.176	1.009	0.606	0.01194
T1 BH	6.066	1746.60	24.7	1.972	1.173	0.0704	0.2800	1.180	1.017	0.639	0.09153
T2 SL	0.752	42.12	25.4	0.087	1.096	0.0415	0.0069	1.094	0.559	0.588	0.00210
T2 SH	1.040	297.80	24.7	0.614	1.096	0.0415	0.0462	1.096	0.566	0.603	0.01481
T2 BL	5.847	318.37	25.4	0.292	1.206	0.0811	0.0519	1.212	1.108	0.572	0.01541
T2 BH	7.880	2316.70	24.7	2.077	1.206	0.0811	0.3760	1.215	1.107	0.568	0.10777

**Table II** Experimental data for determining blockage and inertia corrections, Reynolds number and settling speed ratio. Here the values of  $a_r$  were determined from buoyancy measurements.

Model	$l/a$ (ave.)	V $10^{-6} \text{ m}^3$	A $10^{-4} \text{ m}^2$	$a_r$ $10^{-2} \text{ m}$	$L_s$ $10^{-2} \text{ m}$	$a_r/L_s$ (ave.)	D (@ $T_r$ )	Re (@ $T_r$ )	KS (ave.)	$C_d$
U0A SL	3.60	0.637	4.434	0.534	0.431	1.248	42.06	0.00306	0.894	1.108
U0A SH		0.637	4.434	0.534	0.431		280.11	0.02137		
U0A BL		5.429	18.789	1.090	0.867		364.91	0.02676		
U0A BH		5.429	18.789	1.090	0.867		2255.57	0.15933		
U0B SL	8.00	0.193	2.534	0.358	0.228	1.570	10.76	0.00073	0.790	1.283
U0B SH		0.193	2.534	0.358	0.228		87.17	0.00574		
U0B BL		1.542	10.134	0.717	0.456		99.78	0.00634		
U0B BH		1.542	10.134	0.717	0.456		690.49	0.04439		
U1 SL	3.80	0.796	7.025	0.575	0.340	1.697	43.10	0.00411	0.836	1.178
U1 BL		6.457	28.581	1.155	0.678		374.20	0.03555		
U2 SL	3.80	0.859	7.557	0.590	0.341	1.735	50.86	0.00328	0.807	1.210
U2 SH		0.859	7.557	0.590	0.341		362.38	0.02395		
U2 BL		7.014	30.796	1.188	0.683		413.75	0.02884		
U2 BH		7.014	30.796	1.188	0.683		2965.63	0.19182		
U3 SL	4.40	1.089	10.187	0.638	0.321	1.995	63.58	0.00406	0.785	1.239
U3 SH		1.089	10.187	0.638	0.321		456.40	0.02975		
U3 BL		8.947	41.667	1.288	0.644		469.41	0.03185		
U3 BH		8.947	41.667	1.288	0.644		3735.43	0.22514		
T0A SL	2.67	3.529	15.104	0.944	0.701	1.347	224.05	0.01497	0.825	1.203
T0A SH		3.529	15.104	0.944	0.701		1494.56	0.10253		
T0B BL	4.00	14.80	47.119	1.523	0.942	1.616	983.19	0.05876	0.730	1.377
T0B BH		14.80	47.119	1.523	0.942		6408.24	0.37348		
T0C SL	8.00	0.533	6.745	0.503	0.237	2.122	29.34	0.00144	0.587	1.688
T0C SH		0.533	6.745	0.503	0.237		227.22	0.01101		
T0C BL		4.263	26.981	1.006	0.474		244.53	0.01189		
T0C BH		4.263	26.981	1.006	0.474		1859.90	0.09088		
T1 SL	7.40	0.539	7.817	0.505	0.207	2.438	31.30	0.00161	0.620	1.643
T1 SH		0.539	7.817	0.505	0.207		222.32	0.01121		
T1 BL		4.278	31.039	1.007	0.413		231.79	0.01157		
T1 BH		4.278	31.039	1.007	0.413		1746.25	0.09141		
T2 SL	8.64	0.713	11.733	0.554	0.184	3.007	42.06	0.00204	0.583	1.708
T2 SH		0.713	11.733	0.554	0.184		297.73	0.01479		
T2 BL		5.619	45.876	1.103	0.367		317.87	0.01494		
T2 BH		5.619	45.876	1.103	0.367		2316.27	0.10762		

**Table III** Reduced data for determining the drag *versus* Reynolds number curves and average values of the dendrite shape parameter, settling speed ratio and zero Reynolds number drag coefficient. Here all the geometrical properties in columns 1-6 were determined using the measured physical dimensions in Table I and the surface area and volume formulae derived in Appendix B.

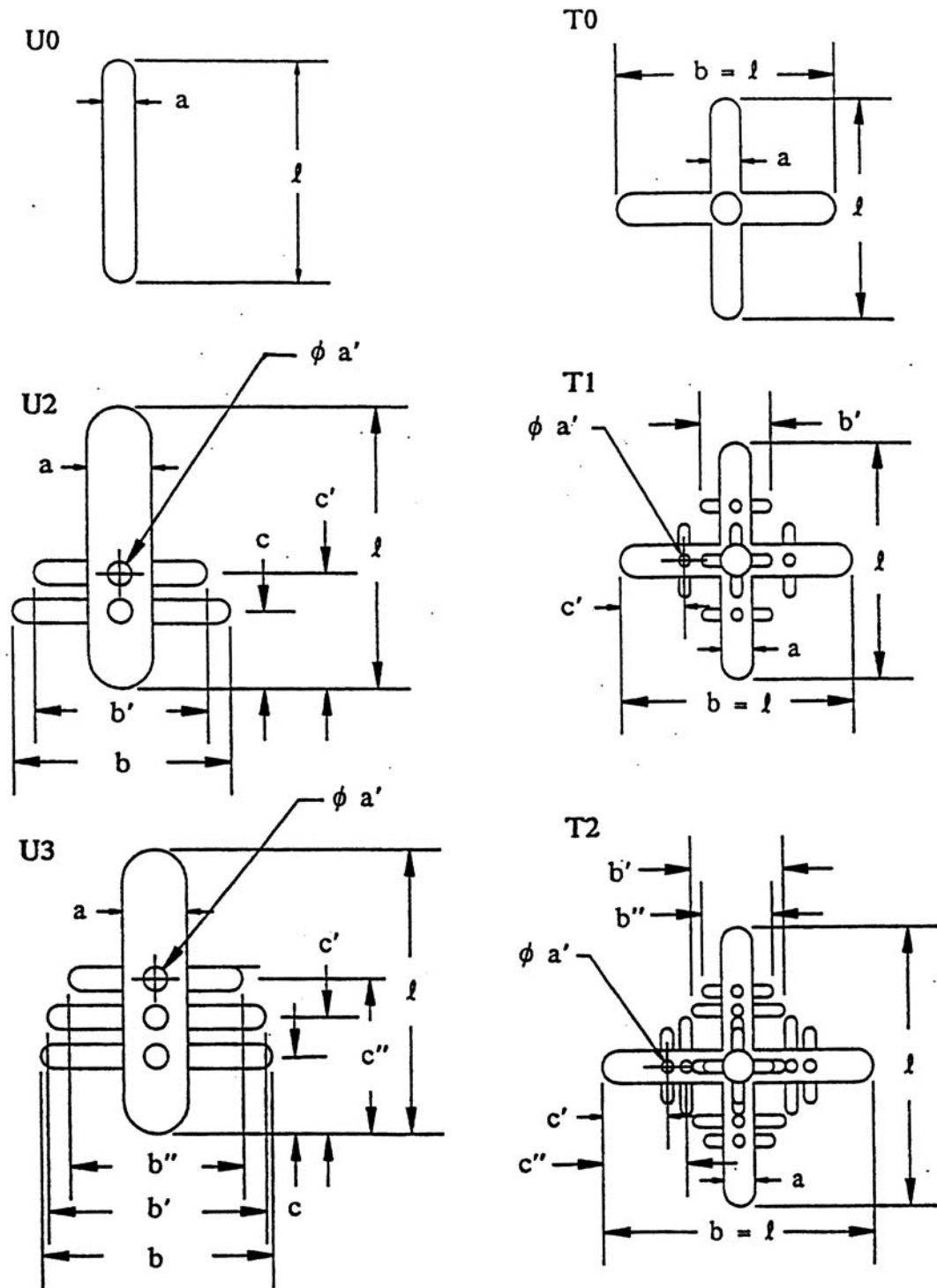


Fig. 1 Six configurations of model dendrite fragments patterned after postsolidification microstructures. U designates the uniaxial series and T designates the triaxial series, and the following number denotes the number of secondary branch systems. All elements comprising the dendrite models are cylindrical rods with rounded hemispherical ends.

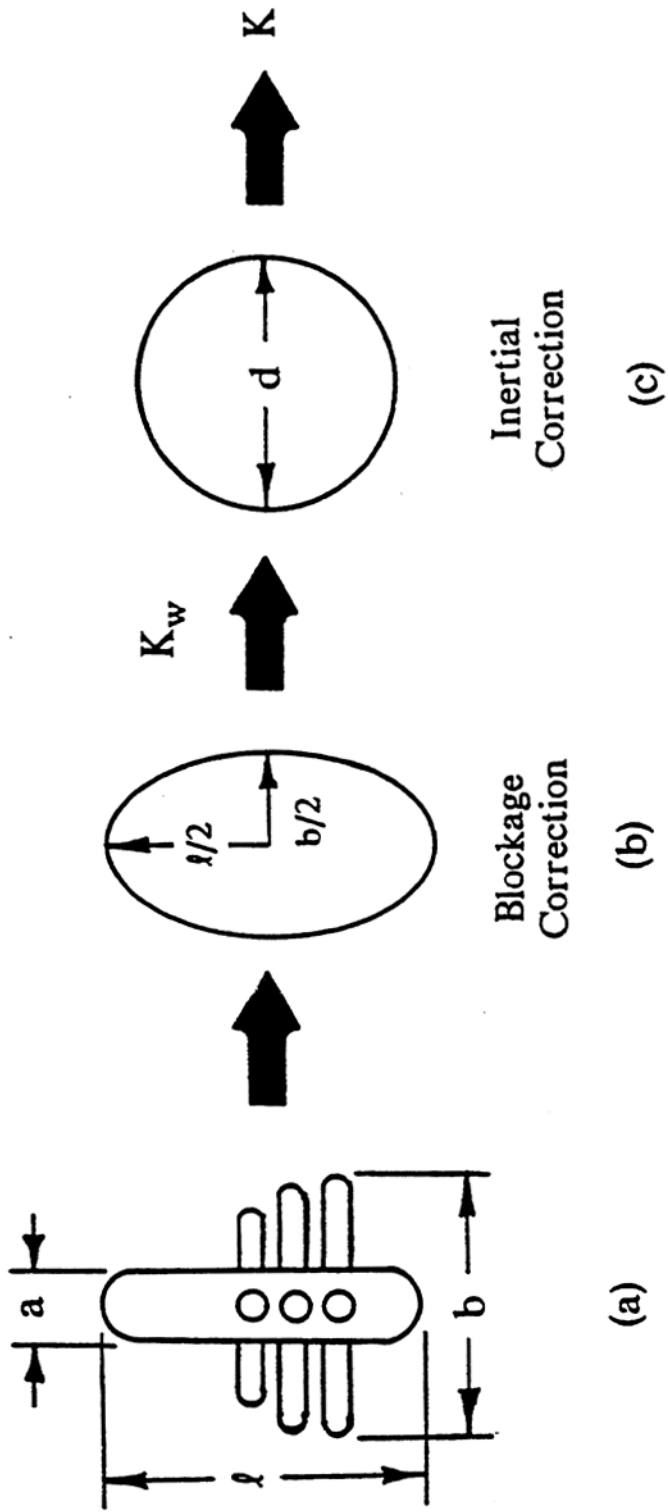


Fig. 2 Schematic diagram outlining the steps employed to compute inertial and blockage corrections for the dendrite models.

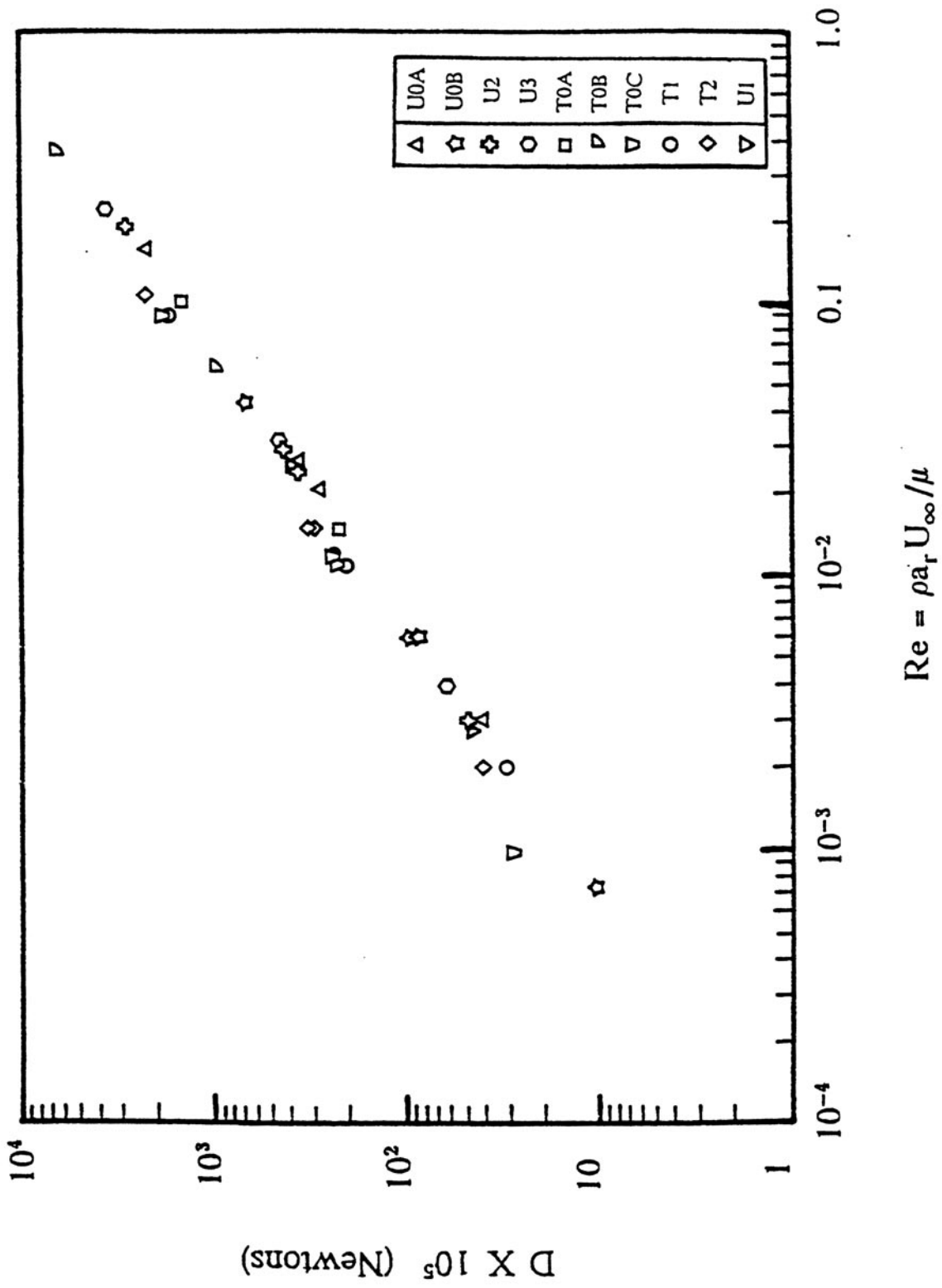
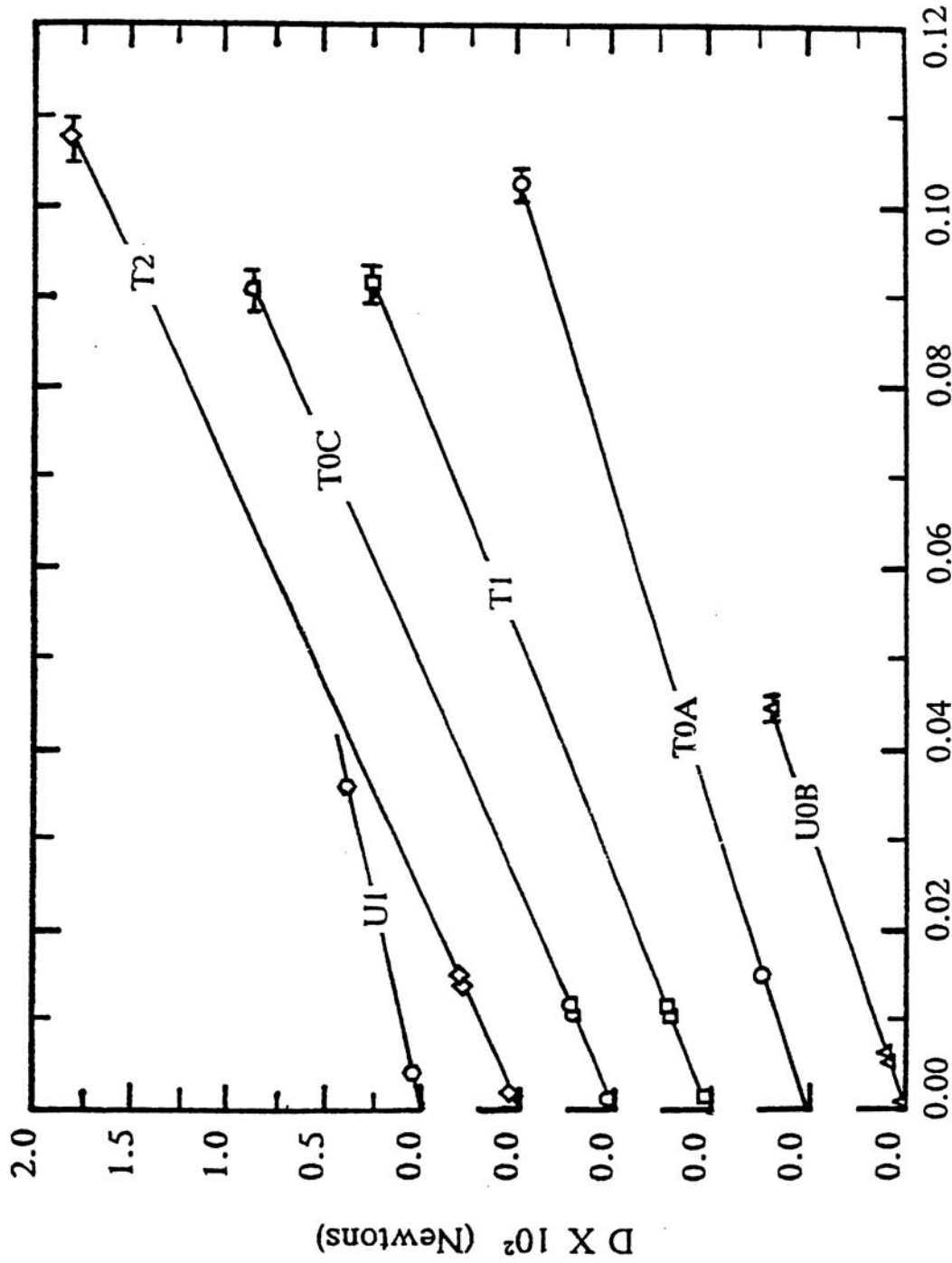


Fig. 3 Log-log plot of drag versus Reynolds number for 34 dendrite models.



$$Re = \rho a_r U_\infty / \mu$$

Fig. 4(a) Drag versus Reynolds number for the lower Reynolds number dendrite groups. The Reynolds number for Model UI tested in a new silicone oil of kinematic viscosity 2.410 kg/m-s was made consistent via the equation  $Re_2 = (\nu_1 \mu_1 / \nu_2 \mu_2) Re_1$ .

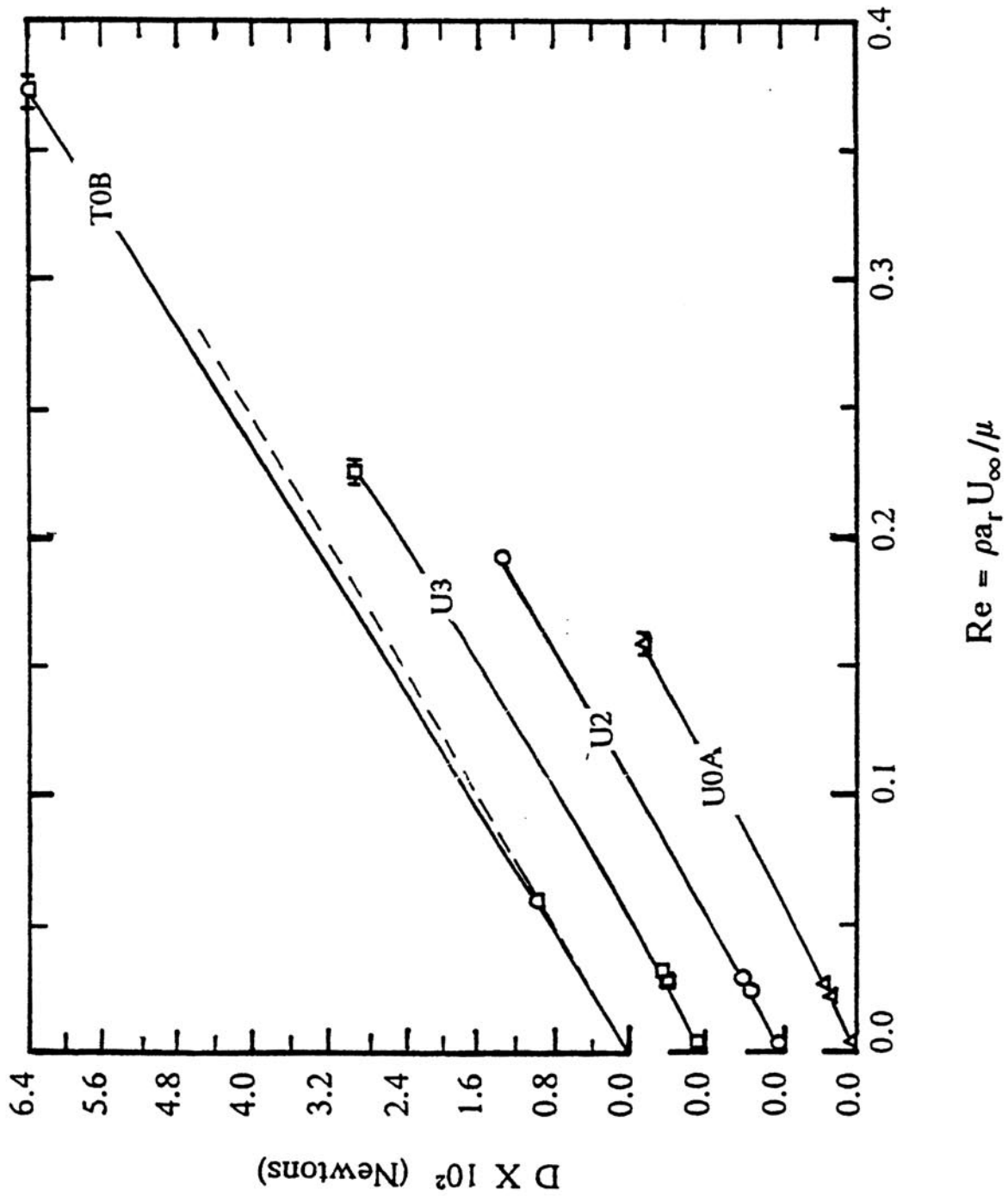


Fig. 4(b) Drag versus Reynolds number for the higher Reynolds number dendrite groups.

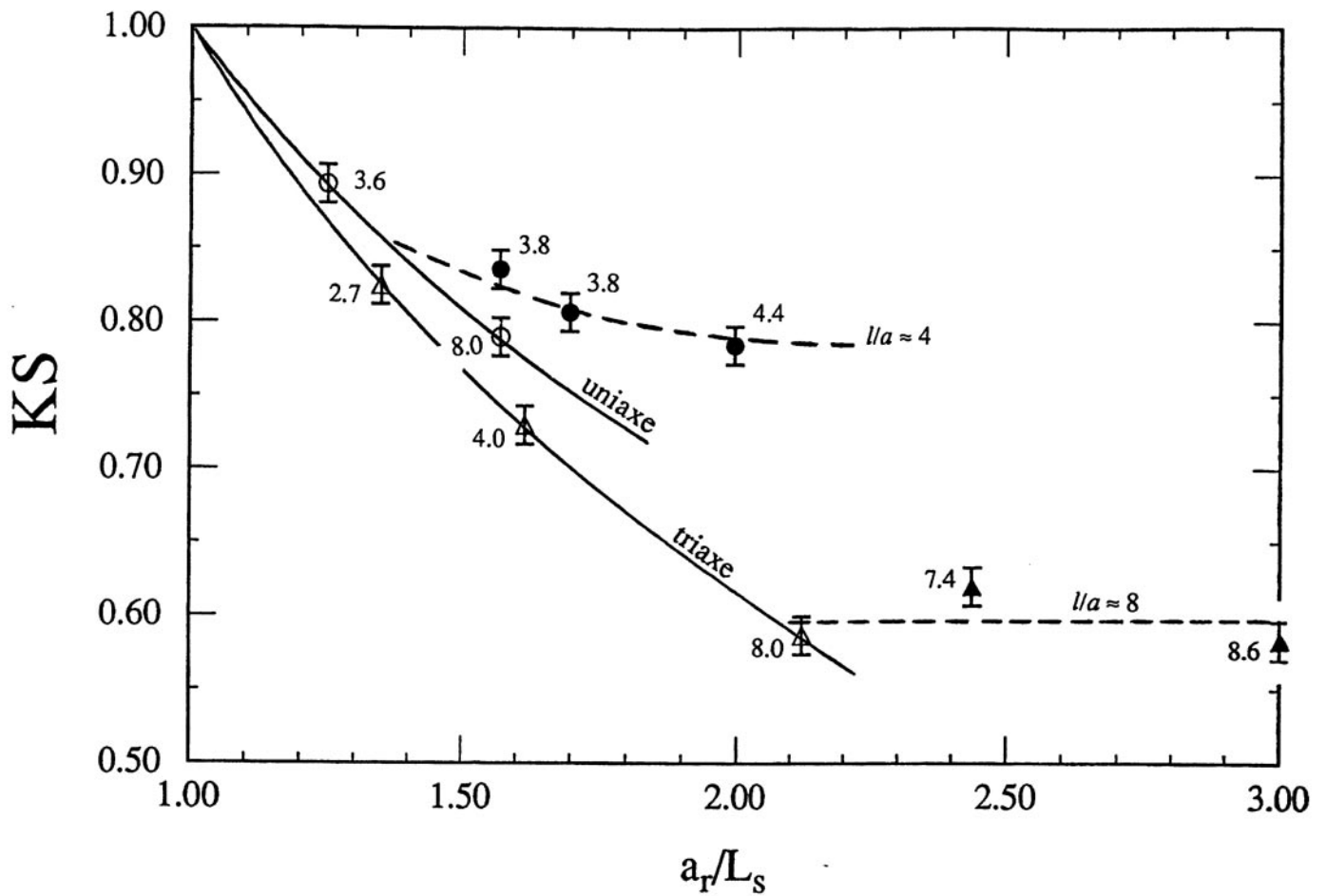


Fig. 5 Settling speed ratio *versus* dimensionless shape parameter for ten self-similar dendrite groups. Circles and triangles correspond to uniaxial and triaxial dendrite models, respectively, and the open symbols refer to branchless dendrites while the closed symbols denote branched systems. Error bars represent the rms deviation of repeated measurements.

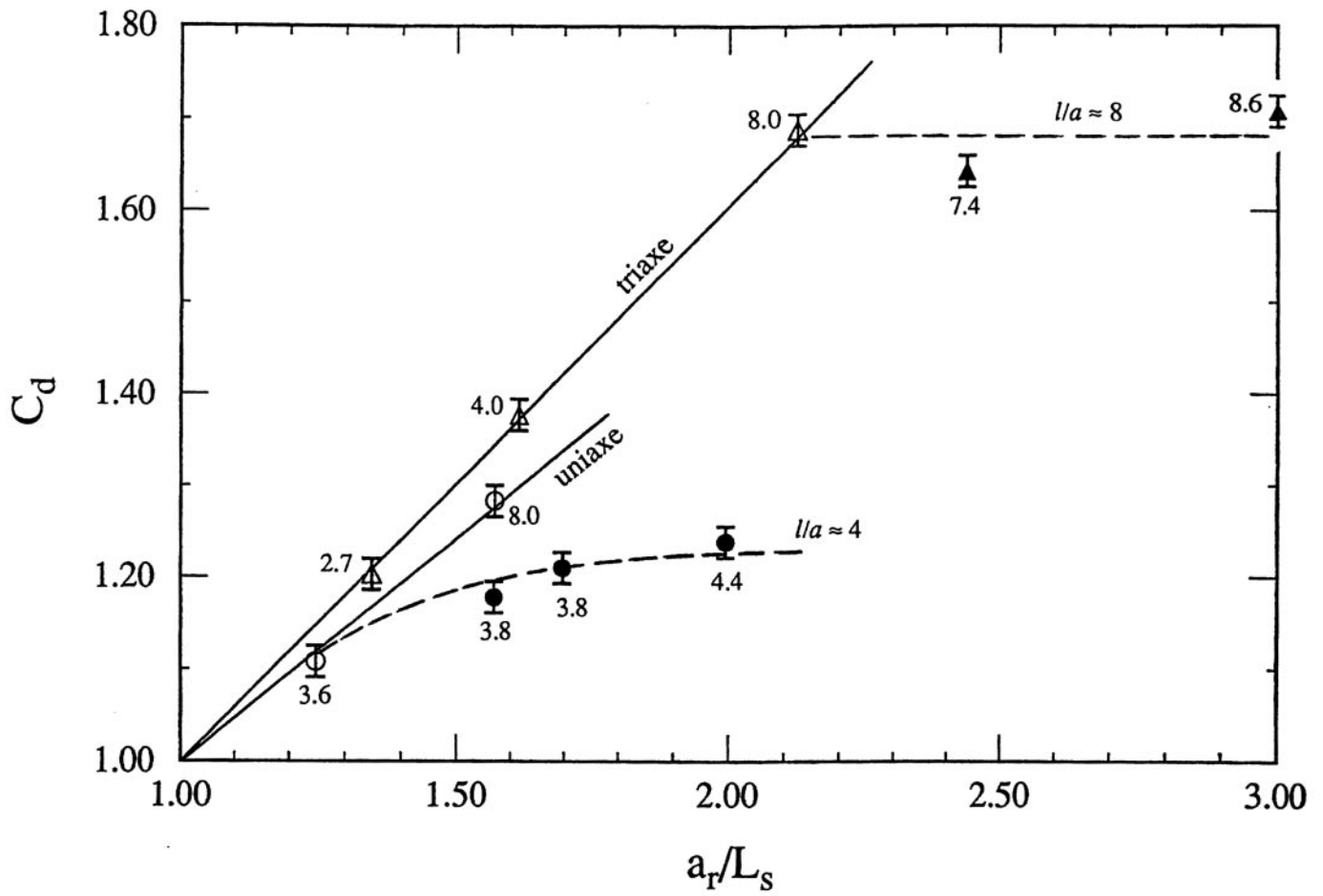


Fig. 6 Zero Reynolds number drag coefficient *versus* dimensionless shape parameter for ten self-similar dendrite groups. See Fig. 5 for symbol definition.

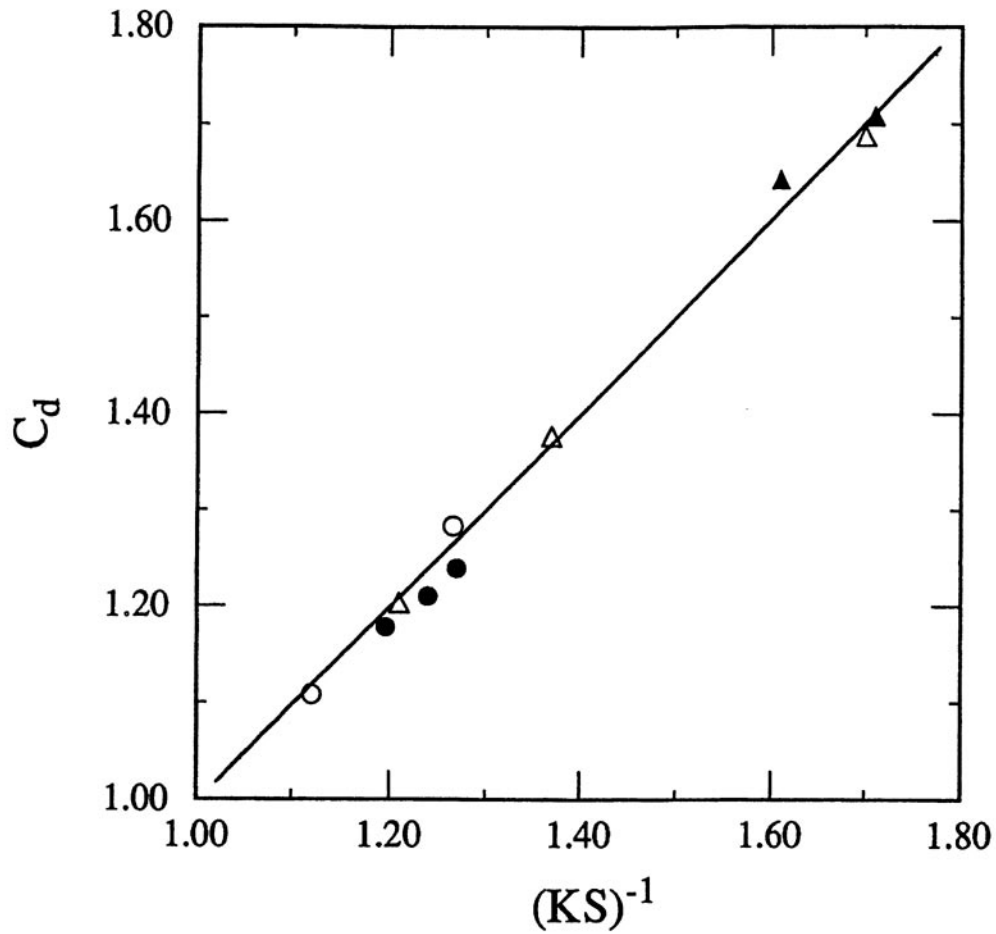


Fig. 7 Drag coefficient obtained from the slope of drag curves in Fig. 4 at zero Reynolds number plotted against the inverse settling speed ratio obtained using the inertial correction procedure of Lasso & Weidman.<sup>[18]</sup> See Fig. 5 for symbol definition.

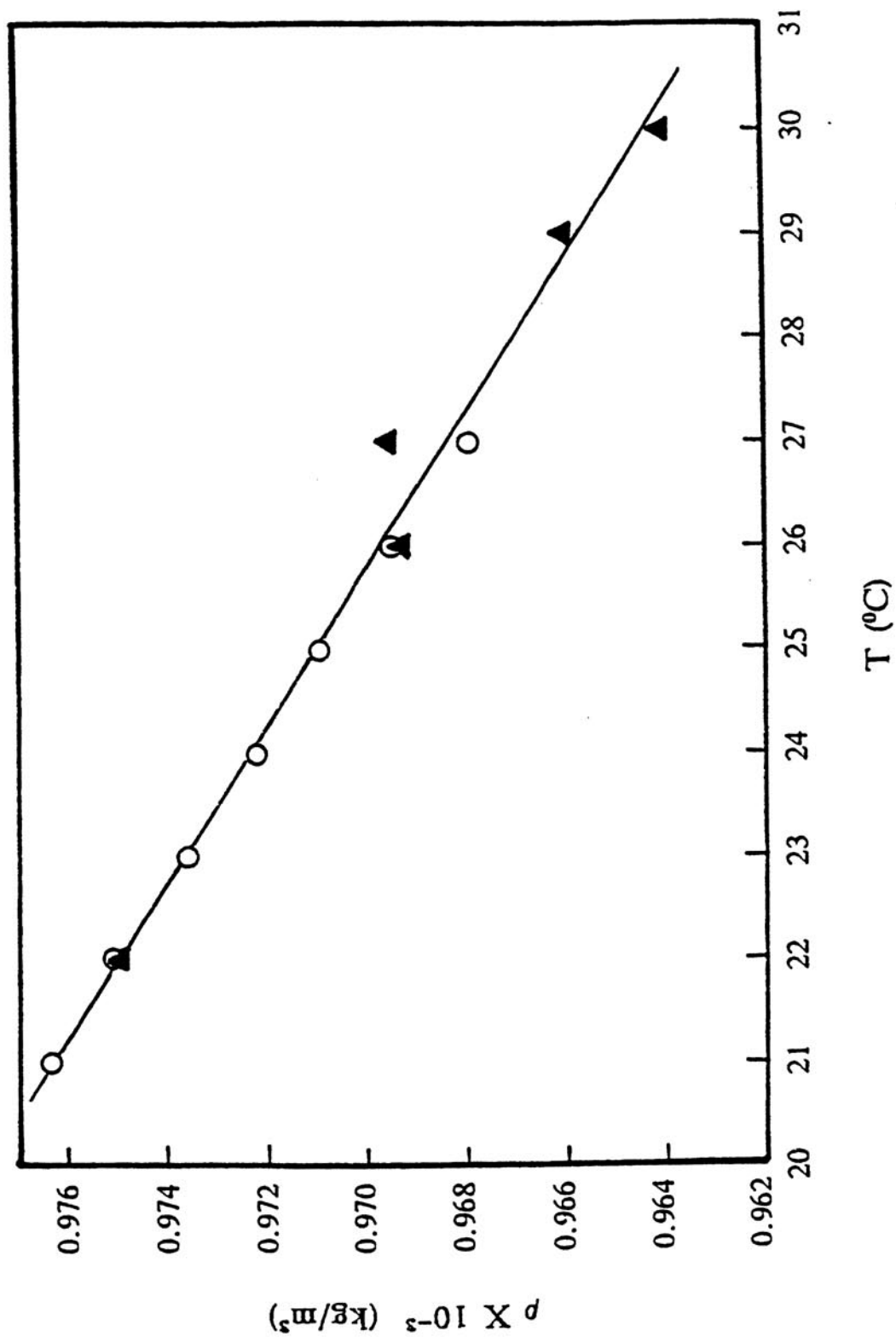


Fig. A1 Density of the silicone oil test liquid as a function of temperature; open circles represent measurements before the test program and solid triangles represent measurements obtained 18 months later.

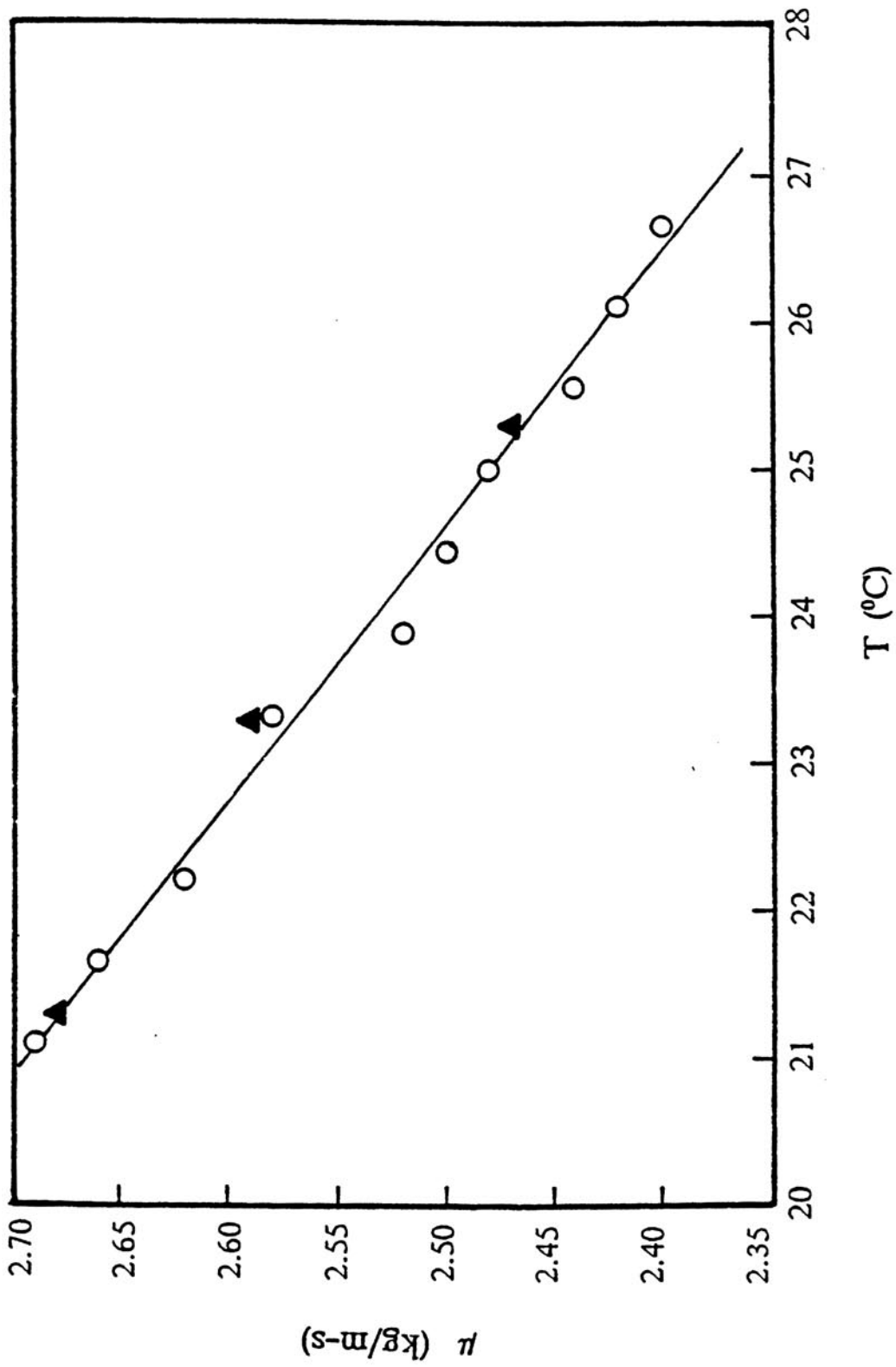


Fig. A2 Dynamic viscosity of the silicone oil test liquid as a function of temperature. See Fig. A1 for symbol definition.

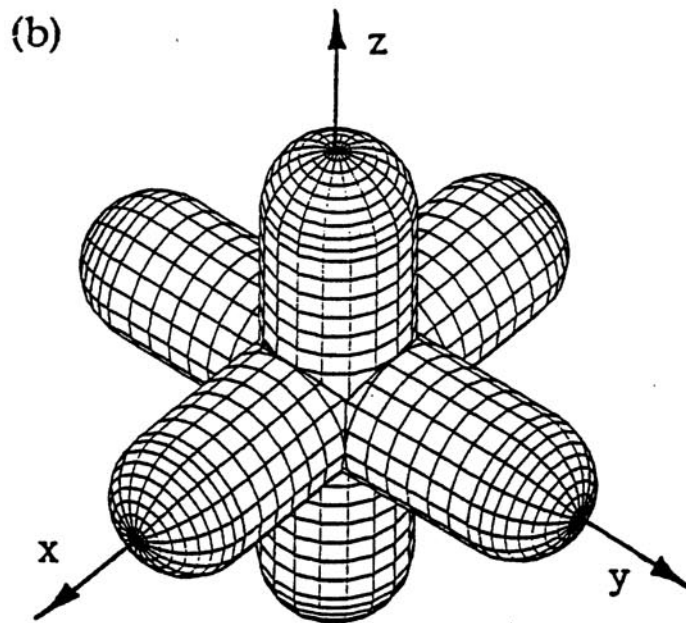
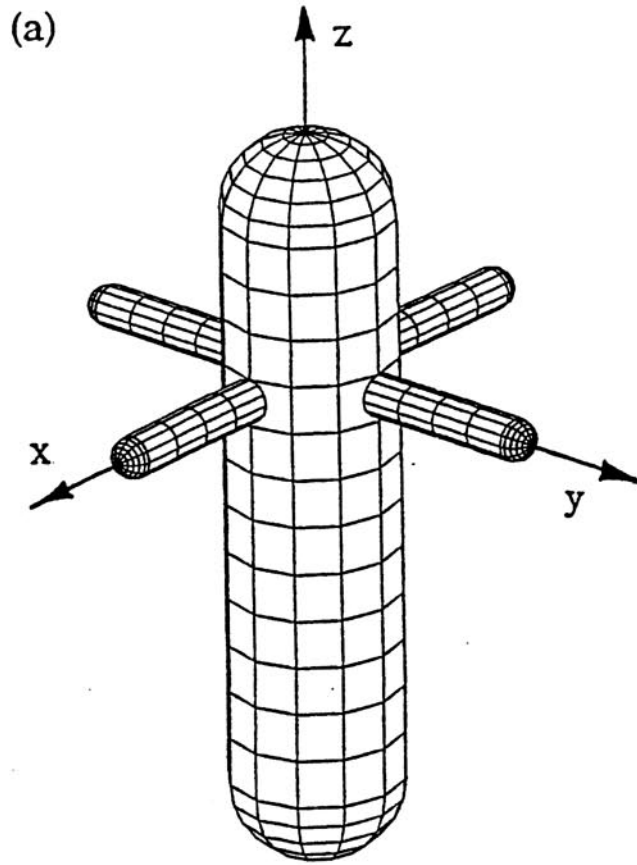


Fig. B1 Oblique views of orthogonally intersecting cylindrical rods; (a) primary rod of radius  $R_2$  intersected by two smaller rods of radii  $R_1$ , and (b) three orthogonally intersecting cylinders of equal radius  $R_2$ .

# REPORT DOCUMENTATION PAGE

*Form Approved*  
OMB No. 0704-0188

Public reporting burden for this collection of information is estimated to average 1 hour per response, including the time for reviewing instructions, searching existing data sources, gathering and maintaining the data needed, and completing and reviewing the collection of information. Send comments regarding this burden estimate or any other aspect of this collection of information, including suggestions for reducing this burden, to Washington Headquarters Services, Directorate for Information Operations and Reports, 1215 Jefferson Davis Highway, Suite 1204, Arlington, VA 22202-4302, and to the Office of Management and Budget, Paperwork Reduction Project (0704-0188), Washington, DC 20503.

<b>1. AGENCY USE ONLY (Leave blank)</b>		<b>2. REPORT DATE</b> February 1993	<b>3. REPORT TYPE AND DATES COVERED</b> Technical Memorandum	
<b>4. TITLE AND SUBTITLE</b>  On the Drag of Model Dendrite Fragments at Low Reynolds Number			<b>5. FUNDING NUMBERS</b>  WU-674-27-05	
<b>6. AUTHOR(S)</b>  R. Zakhem, P.D. Weidman, and H.C. de Groh III				
<b>7. PERFORMING ORGANIZATION NAME(S) AND ADDRESS(ES)</b>  National Aeronautics and Space Administration Lewis Research Center Cleveland, Ohio 44135-3191			<b>8. PERFORMING ORGANIZATION</b>  E-7583	
<b>9. SPONSORING/MONITORING AGENCY NAME(S) AND ADDRESS(ES)</b>  National Aeronautics and Space Administration Washington, DC 20546-0001			<b>10. SPONSORING/MONITORING</b>  NASA TM-105916	
<b>11. SUPPLEMENTARY NOTES</b> R. Zakhem and P.D. Weidman, University of Colorado, Department of Mechanical Engineering, Boulder, Colorado, 80309 and H.C. de Groh III, NASA Lewis Research Center. Responsible person, H.C. de Groh III, (216) 433-5025.				
<b>12a. DISTRIBUTION/AVAILABILITY STATEMENT</b>  Unclassified - Unlimited Subject Category 26			<b>12b. DISTRIBUTION CODE</b>	
<b>13. ABSTRACT (Maximum 200 words)</b>  An experimental study of low Reynolds number drag on laboratory models of dendrite fragments has been conducted. The terminal velocities of the dendrites undergoing free fall along their axis of symmetry were measured in a large Stokes flow facility. Corrections for wall interference give nearly linear drag versus Reynolds number curves. Corrections for both wall interference and inertia effects show that the dendrite Stokes settling velocities are always less than that of a sphere of equal mass and volume. In the Stokes limit, the settling speed ratio is found to correlate well with the primary dendrite arm aspect ratio and a second dimensionless shape parameter which serves as a measure of the fractal-like nature of the dendrite models. These results can be used to estimate equiaxed grain velocities and distance of travel in metal castings. The drag measurements may be used in numerical codes to calculate the movement of grains in a convecting melt in an effort to determine macrosegregation patterns caused by the sink/float mechanism.				
<b>14. SUBJECT TERMS</b> Dendrite; Stokes settling; Dendrite settling; Macrosegregation; Dendrite volume; Dendrite surface area			<b>15. NUMBER OF PAGES</b> 36	
			<b>16. PRICE CODE</b> A03	
<b>17. SECURITY CLASSIFICATION</b> Unclassified	<b>18. SECURITY CLASSIFICATION</b> Unclassified	<b>19. SECURITY CLASSIFICATION</b> Unclassified	<b>20. LIMITATION OF ABSTRACT</b>	